Nanometer-Scale Spatial and Spectral Mapping of Exciton Polaritons in Structured Plasmonic Cavities

Marc R. Bourgeois,[1] Elliot K. Beutler,[1] Siamak Khorasani,[2] Nicole Panek,[1] and David J. Masiello[1,2,*]
[1]Department of Chemistry, University of Washington, Seattle, Washington 98195, USA
[2]Department of Materials Science and Engineering, University of Washington, Seattle, Washington 98195, USA

(Received 21 November 2021; accepted 6 April 2022; published 12 May 2022)

Exciton polaritons (EPs) are ubiquitous light-matter excitations under intense investigation as test beds of fundamental physics and as components for all-optical computing. Owing to their unique attributes and facile experimental tunability, EPs potentially enable strong nonlinearities, condensation, and superfluidity at room temperature. However, the diffraction limit of light and the momentum content of fast electron probes preclude the characterization of EPs in nanoscale structured cavities exhibiting energy-momentum dispersion. Here we present fully relativistic analytical theory and companion numerical simulations showing that these limitations can be overcome to measure EPs in periodic nanophotonic cavities on their natural energy, momentum, and length scales via lattice electron energy gain spectroscopy. With the combined high momentum resolution of light and nanoscale spatial resolution of focused electron beams, lattice electron energy gain spectroscopy can expose deeply subwavelength EP features using currently available monochromated, aberration-corrected scanning transmission electron microscopes.

DOI: 10.1103/PhysRevLett.128.197401

Exciton polaritons (EPs) are hybrid light-matter quasiparticles formed via the strong coupling of an optical cavity mode to ensembles of quantum emitters. Direct polariton-polariton interactions inherited from the excitonic component underlie phenomena such as Bose-Einstein condensation [1,2] and superfluidity [3] of EPs, while comparatively strong nonlinearities have enabled polariton-based all-optical switches [4] and transistors [5,6]. Meanwhile, the photon component is responsible for the low polariton effective mass and enables long-range transport properties [7]. There is also much interest in the potential of polaritonic effects to modify chemical reaction dynamics [8–12], however, the mechanistic details remain somewhat controversial [13–15]. Together, these fundamental features and potential technological applications have conspired to prompt intense research efforts to understand and to leverage the unique properties of EPs.

Early work on EPs mainly employed planar microcavity architectures with the excitonic medium positioned at an antinode of the cavity field. The uniformity of the cavity field strength in the directions transverse to the microcavity axis causes each of the N emitters in the ensemble to experience nearly equal cavity-coupling strengths such that the resulting EPs are well described by the Tavis-Cummings model with Rabi splitting $\propto \sqrt{N}$. Besides microcavities, recent advances have relied upon expanding the catalog of cavity architectures [16,17]. Metal nanoparticles (NPs) supporting localized surface plasmons (LSPs) have emerged as a promising material platform owing, in part, to their small mode volumes. Plasmonic NP-based structures have, e.g., been utilized in demonstrations of the strong coupling regime in the single emitter limit [18]. While increasing the number of emitters participating in the formation of plasmon EPs increases apparent spectral splitting, strong spatial variation of the electric field strength outside the NPs necessarily leads to position-dependent exciton-cavity coupling strengths that violate the equal-coupling strength assumption of the Tavis-Cummings model [9].

A related cavity architecture consists of periodic arrays of plasmonic NPs, which host lattice plasmon polaritons (LPPs) arising from the hybridization of the diffractive photonic modes inherited from the array periodicity with the LSPs supported by each NP [19–21]. Unlike LSP excitations, LPPs exhibit strong energy-momentum dispersion inherited from the diffractive photonic component [22]. Despite this critical difference, Rabi splitting in the strong coupling regime has been demonstrated for LPPs coupled to ensembles of emitters of various types [23–29]. In both LSP- and LPP-based systems, the nanometer-scale spatial variation of the cavity-emitter coupling strength has made direct spatial mapping of plasmon EPs experimentally challenging using diffraction-limited optical techniques. Near-field based imaging techniques such as s-SNOM have been used to probe EPs in systems involving LSPs [30], as well as to probe the energy-momentum dispersion of polaritons involving atomic crystals, including hBN phonon polaritons [31], graphene plasmons [32], and transition-metal dichalcogenide exciton polaritons [33], but has not yet been used to measure EPs in LPP-based systems. Alternatively, recent advances in energy monochromation and aberration correction in

state-of-the-art scanning transmission electron microscopes (STEMs) have made it possible to map plasmon EPs on their natural energy and length scales using electron energy-loss spectroscopy (EELS) [34,35].

Here we show that while the energy-momentum dispersion fundamental to LPPs precludes the use of STEM EELS for spatial mapping of LPP EPs, closely related laser-stimulated lattice electron energy gain (LEEG) measurements are well suited to the task. Specifically, based on analytic and numerical analysis of the relativistic quantum mechanical LEEG probability from an optically excited NP array we establish that LEEG measurements can probe LPPs and LPP EPs with simultaneously high momentum, energy, and spatial resolution both in the absence and presence of coupling to excitonic emitters. Spatial maps of excited LPP EPs are achievable with nanometer spatial resolution by raster scanning the STEM electron beam within the array unit cell, while various points in the LPP-EP band structure can be probed with high momentum resolution by varying the optical excitation angle of incidence. The proposed experiment unlocks the door to a detailed view into the complex makeup of EPs in structured cavity systems; LEEG measurements provide the energy and spatial resolution required to directly resolve subdiffraction-limited spatial structure in LPP EPs.

We first investigate the 1D NP array displayed in Fig. 1(a) in the absence of the excitonic medium. The array is composed of identical 90 nm diameter Ag spherical NPs oriented along $\hat{\mathbf{y}}$ with periodicity $a = 415$ nm in vacuum. Signatures of the reciprocal space LPPs arising from coupling of the electric dipole LSP near 3.25 eV (solid white) to the photonic diffraction modes dictated by the array periodicity (dashed white) are clearly evident in the $K_{||}$-dependent per-unit cell extinction efficiency spectra $\bar{\sigma}_{\mathrm{ext}}(\omega)$ in Fig. 1(b). Importantly, the LPPs inherit the energy-momentum dispersion of the ± 1 diffraction orders with the strongest LPP excitation occurring at the Γ point ($K_{||} = 0$).

In a STEM EEL measurement, the electron trajectory can be oriented either perpendicular ($e_{\perp}^{-}$) or parallel ($e_{||}^{-}$) to the array as depicted in Fig. 1(a). With its lateral spatial confinement and ability to raster scan the electron beam throughout the unit cell, the $e_{\perp}^{-}$ trajectory seems ideal for EP mapping. Indeed, this geometry was recently employed to image EPs formed by coupling WS_2 excitons to plasmonic triangular nanoprisms [35]. However, Fig. 1(c) shows the reduced loss function $\tilde{\Gamma}_{\mathrm{EEL}}^{N=501}(\omega)$, i.e., $\Gamma_{\mathrm{EEL}}^{N}(\omega)$ normalized by the maximum value of $\Gamma_{\mathrm{EEL}}^{N=1}(\omega)$, of a finite array with $N = 501$ NPs (solid red) is nearly indistinguishable from that of an individual NP $\tilde{\Gamma}_{\mathrm{EEL}}^{N=1}(\omega)$ (solid black). While the $K_{||} = 0$ LPP just below 3.0 eV is clearly evident in the reduced optical extinction spectrum $\tilde{\sigma}_{\mathrm{ext}}(\omega)$ (dashed gray), the inset in Fig. 1(c) shows only weak features at this energy in the EEL observable. The weak signatures of reciprocal space LPP modes in the $e_{\perp}^{-}$ EEL spectra can be traced back to the transverse spatial confinement of the electron beam and the energy-momentum dispersion of the LPPs (SM). With the broadband spatial and spectral character of their field

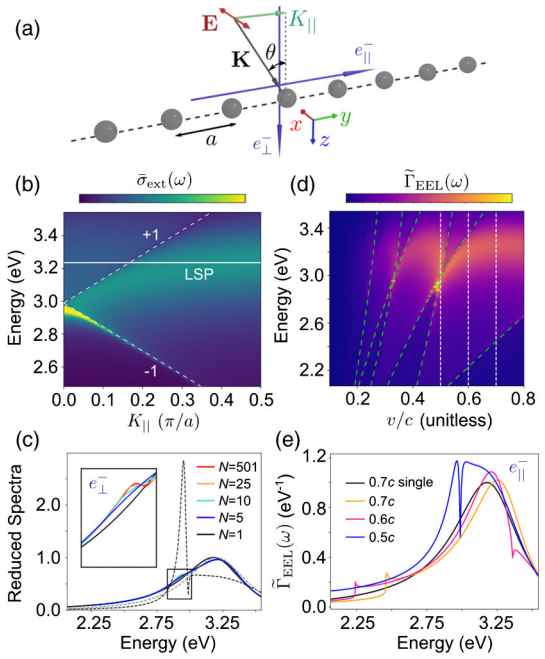

FIG. 1. Optical and electron excitation of 1D arrays. (a) Scheme of 1D array excited by a plane wave and/or a focused electron beam with trajectory parallel or perpendicular to the lattice periodicity direction. (b) Per-NP optical extinction spectra for an infinite 1D array of 90 nm diameter Ag NPs with periodicity $a = 415$ nm as a function of $K_{||}$. The solid line denotes the energy of the isolated NP dipolar LSP, while the dashed lines mark the energy-momentum dispersion of the ± 1 photonic diffraction orders. (c) $\tilde{\Gamma}_{\mathrm{EEL}}^{N}(\omega)$ for a $0.7c$ electron moving along the perpendicular trajectory versus the number of NPs N in finite array realizations. The normalized optical extinctions of the single NP (dashed gray line) and array (dashed black line; $N = 501$) are displayed for reference. (d) $\tilde{\Gamma}_{\mathrm{EEL}}(\omega)$ for an electron moving along the parallel trajectory with $N = 501$ versus velocity. (e) Line out spectra from (d) at the dashed vertical lines. In panels (c)–(e) the electron trajectory passes 5 nm outside of the NP surface.

$$\mathbf{E}_e(\mathbf{x},t) = \frac{ie}{2\pi^2 v}\int d\mathbf{q}_{\perp} d\omega \frac{(\mathbf{q}_{\perp}, \omega/\gamma_L^2 v)}{q_{\perp}^2 + (\omega/\gamma_L v)^2} e^{i\mathbf{q}_{\perp}\cdot\mathbf{R}} e^{-i\omega(t-z/v)}, \tag{1}$$

STEM electrons excite a broad superposition of reciprocal space LPP modes, and since the band edge LPP is highly localized in reciprocal space at $K_{||} = 0$, only a weak signature survives once the integration over $\mathbf{q}_{\perp}$ (and hence $K_{||}$ of the NP array) is performed at each energy. Here, $\mathbf{x} = (\mathbf{R}, z)$ and $\gamma_L = 1/\sqrt{1-(v/c)^2}$ is the Lorentz contraction factor with electron speed v. One possibility to overcome this

issue is to employ momentum-resolved EEL spectroscopy [36–39]; however, state-of-the-art momentum resolution is $\Delta q \approx 0.025\ \text{Å}^{-1} = 0.25\ \text{nm}^{-1}$ [39], which is not sufficient to resolve typical photonic cavity band structures. For example, the full extent of the Brillouin zone for a periodic structure with $a = 415$ nm is $\Delta q_{\text{BZ}} = 2\pi/(415\ \text{nm}) \approx 0.015\ \text{nm}^{-1}$.

In the $e_{||}^{-}$ geometry the STEM electron travels parallel to the array direction with its momentum along the array's Bloch wave vector $K_{||}$. Band folding provides opportunities for the electron to exchange energy and momentum with the LPPs despite the electron momentum transfer dispersion lying below the free space light line (SM). Consequently, the electron can couple to free space radiation, known as Smith-Purcell radiation [40,41], and the observed loss spectra $\tilde{\Gamma}_{\text{EEL}}(\omega)$ acquire a strong dependence on the electron velocity as shown in Fig. 1(d). Figure 1(e) displays EEL spectra for $v = 0.5c$, $0.6c$, and $0.7c$ [marked by vertical dashed lines in Fig. 1(d)]. Each of these loss spectra is similar to that of the isolated NP (black) except in the vicinity of the dashed green lines in Fig. 1(d), which denote the points in $E - v$ space where Smith-Purcell radiation occurs (SM). Besides losing the ability to raster scan the impact parameter through the unit cell to map the LPP spatial distribution, the $e_{||}^{-}$ geometry also requires careful tuning of the electron velocity to sample different regions of the LPP dispersion diagram. Together, the various disadvantages of these $e_{\perp}^{-}$ and $e_{||}^{-}$ geometries preclude the use of STEM EELS to spatially map EPs in structured cavities, thereby motivating exploration of alternative measurement strategies.

One such technique is that of laser-stimulated EEG spectroscopy, originally proposed by Howie [42] and subsequently developed theoretically [43,44], whereby the energy $\hbar\omega$ gained by a STEM electron interacting with an optically excited target is measured. At first order in perturbation theory under the nonrecoil approximation, the probability is [43]

$$\mathcal{P}_{\text{EEG}}(\omega) = \left(\frac{e}{\hbar\omega}\right)^2 \left| \int dz \hat{\mathbf{z}} \cdot \mathbf{E}(\mathbf{R}_e, z) e^{-i\omega z/v} \right|^2, \quad (2)$$

where $\mathbf{v} = \hat{\mathbf{z}} v$ and $\mathbf{E}(\mathbf{R}_e, z)$ is the target's optical response field. In the case of the 1D array excited by an x-polarized plane wave, the LEEG probability becomes (SM)

$$\mathcal{P}_{\text{EEG}}(\omega) = \left(\frac{2e\omega}{\hbar\gamma_L v^2}\right)^2 |\Pi_{xx}(K_{||}, \omega)|^2 \frac{2\pi}{c} I_0 \times \left| \sum_n (\hat{\mathbf{x}} \cdot \hat{\mathbf{R}}_{en}) K_1\left(\frac{\omega R_{en}}{\gamma_L v}\right) e^{iK_{||} n a} \right|^2, \quad (3)$$

where I_0 is the incident laser intensity, K_1 is a modified Bessel function of the second kind, and $\mathbf{R}_{en}$ is the vector from the nth NP in the array to the electron trajectory in the xy plane. Unlike in EEL and cathodoluminescence measurements [45–47], LEEG occurs only at the specific Brillouin zone points excited by the optical field and does not inherit the full $(\mathbf{q}_{\perp}, \omega)$ dispersion of the STEM electron. Because of the rapid decay of $K_1(x)$, retaining only $n = 0$ is a good approximation to $\mathcal{P}_{\text{EEG}}$ for impact parameters close to the NP. This approximation yields an expression identical to the EEG response of a single NP [43,44] with the isolated particle dipole polarizability tensor $\overleftrightarrow{\alpha}(\omega)$ replaced by the nonlocal lattice-dressed polarizability tensor $\overleftrightarrow{\Pi}(K_{||}, \omega) = [\overleftrightarrow{\alpha}^{-1}(\omega) - \overleftrightarrow{S}(K_{||}, \omega)]^{-1}$, [21] where $\overleftrightarrow{S}(K_{||}, \omega)$ is the lattice sum tensor accounting for electromagnetic coupling among particles in the array. LPPs are encoded by the poles of $\overleftrightarrow{\Pi}(K_{||}, \omega)$ (SM).

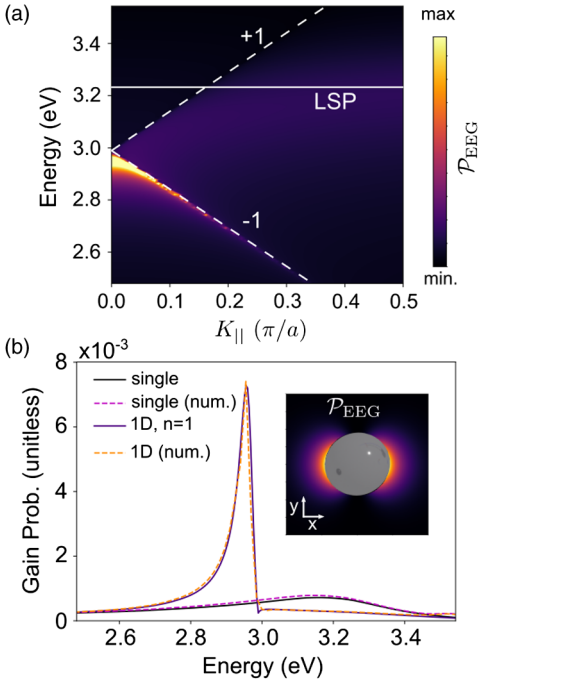

FIG. 2. Lattice electron energy gain spectroscopy. (a) Analytic LEEG probability spectra for the same Ag NP array as a function of $K_{||}$. (b) Analytical (solid) and numerical (dashed) evaluation of $\mathcal{P}_{\text{EEG}}$ spectra for a single particle and 1D array. Inset shows a spatial map of $\mathcal{P}_{\text{EEG}}$ at the LPP energy around one particle. Here, $v = 0.7c$ and $I_0 = 10^9\ \text{W/cm}^2$.

Figure 2(a) shows lattice $\mathcal{P}_{\text{EEG}}(\omega)$ spectra calculated using the $n = 0$ approximation with electron trajectory along $\hat{\mathbf{z}}$ and an impact factor 5 nm outside the NP surface along $\hat{\mathbf{x}}$ as a function of $K_{||}$. Unlike EEL, LEEG probes a specific point in reciprocal space dictated by $K_{||}$ of the incident plane wave and the optically induced LPP dispersion of Fig. 1(b) is clearly evident in the LEEG spectra in Fig. 2(a). In particular, $\mathcal{P}_{\text{EEG}}(\omega)$ for the 1D array at $K_{||} = 0$ exhibits a strong contribution from the band edge LPP that is significantly enhanced relative to the maximum gain probability of the isolated NP as shown in Fig. 2(b).

The single NP and 1D array spectra calculated analytically (solid traces) were validated against a fully numerical evaluation of $\mathcal{P}_{\mathrm{EEG}}(\omega)$ using Eq. (2) together with optical response fields $\mathbf{E}(\mathbf{R}_e, z)$ from periodic coupled-dipole calculations [48] (dashed traces). Importantly, the simultaneous energy and reciprocal-space resolution of LEEG does not come at the expense of spatial resolution. The inset in Fig. 2(b) shows a spatial map of $\mathcal{P}_{\mathrm{EEG}}(\omega)$ at the energy of the $K_{||} = 0$ LPP within the unit cell.

Having demonstrated the unique advantages of LEEG spectroscopy for spatially mapping LPP excitations in NP arrays, we now consider LPP EPs that can emerge for a 1D Ag NP array embedded in an excitonic slab medium modeled using a Lorentz dielectric function $\varepsilon(\omega) = 1 + f\omega_0^2/(\omega_0^2 - \omega^2 - i\gamma\omega)$, where ω_0 is the exciton transition frequency, γ is the exciton damping rate, and f is an effective oscillator strength. Note that while this is a standard approach for accounting for the exciton response in strong coupling systems with macroscopic numbers of emitters [24,28,29,34,49], this form of the exciton medium response is equivalent to replacing the discrete two-level system emitters by classical oscillators, which is a good approximation in the low excitation limit [50]. In experiments, the Rabi splitting observable in the strong coupling regime can be varied by either increasing the emitter's transition dipole moment, or the concentration of emitters within the mode volume. Within the context of the Lorentz model, both are equivalent to increasing the value of the effective oscillator strength f.

Figure 3(a) shows the response field within a unit cell of the 1D array excited at $K_{||} = 0$ with x-polarized light and $f = 0$, demonstrating the strong spatial variation of the cavity field. Figure 3(b) presents numerically calculated normalized LEEG probabilities $\mathcal{P}_{\mathrm{EEG}}(\omega)$ (dashed) and normalized point absorption spectra $\sigma_{\mathrm{abs}}(\omega)$ proportional to $\omega\mathrm{Im}[\varepsilon(\omega)]|\mathbf{E}(\mathbf{R}, z)|^2$ at $z = 0$ (solid) in the presence of the excitonic slab at points marked P1 and P2 in Fig. 3(a) versus f. P1 and P2 were selected as they are near an antinode and node of the cavity field in the xy plane at $z = 0$. Note that $\mathcal{P}_{\mathrm{EEG}}(\omega)$ depends only on the component of the response field polarized along the electron trajectory, while $\sigma_{\mathrm{abs}}(\omega)$ depends on all three Cartesian components. To reduce spurious edge effects arising from the finite transverse width of the slab in the x direction, we employed a background subtraction procedure for the LEEG spectra in Fig. 3(b) (SM). In addition to a peak near the uncoupled exciton energy $\hbar\omega_0$ (vertical black dashed line), the point absorption spectra at P1 clearly show the upper polaritons (UPs) and lower polaritons (LPs)with an energy splitting that increases with f, which aligns with expectations based on the empty-lattice dispersion relation with a dispersive embedding medium (SM). Although the background subtraction procedure for $\mathcal{P}_{\mathrm{EEG}}(\omega)$ removes the contribution at the uncoupled exciton energy, signatures from the UPs and LPs are evident at energies slightly above and below those

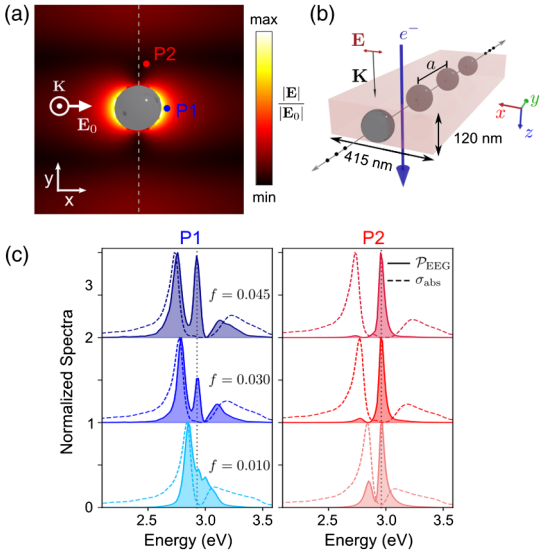

FIG. 3. Position-dependent LEEG probability and point absorption spectra for the same 1D array embedded inside an excitonic medium. (a) Spatial distribution of the optically excited electric field within the xy plane in the absence of the emitter medium. The dashed gray line indicates the array axis. (b) Scheme showing the 1D array inside the emitter medium slab. (c) Normalized $\mathcal{P}_{\mathrm{EEG}}$ (dashed) and σ_{abs} (solid) spectra at points P1 and P2 in panel (a) for the 1D array inside excitonic media of varying f. The vertical dotted lines at 2.95 eV mark the resonance energy of the bulk excitonic transition $\hbar\omega_0$.

observed in the absorption spectra since $\mathcal{P}_{\mathrm{EEG}}(\omega)$ is a scattering measurement [49,51] and includes the additional effects of radiation damping and interference. At P2 the cavity field is suppressed and absorption occurs primarily at $\hbar\omega_0$ with weaker features appearing in $\sigma_{\mathrm{abs}}(\omega)$ at the UP and LP energies observed at P1.

Figure 4(a) shows the relative $\mathcal{P}_{\mathrm{EEG}}(\omega)$ and $\sigma_{\mathrm{abs}}(\omega)$ spectra at P1 and P2 for the combined array-slab ($f = 0.0445$) system, i.e., the spectra at P1 and P2 each normalized by the maximum value at P1. While the spectra at P2 have the same shape as those observed at P1, the UP and LP amplitudes are considerably reduced. Although the demonstration of Rabi splitting in absorption is a more appropriate indication of strong coupling [35,49,51], local absorption measurements on the nanoscale remain experimentally challenging [52–55] and dark-field scattering is often easier to obtain for LSP-based systems. Despite measuring a scattering response, the variation in the $\mathcal{P}_{\mathrm{EEG}}(\omega)$ amplitudes at the UP and LP energies can be used to create spatial maps of the optically excited LPP EPs as the STEM electron beam is raster scanned throughout the unit cell. Similar to what has been observed for LSP EPs [35], both sets of spectrum images in Figs. 4(b) and 4(c) exhibit a characteristic dipole distribution indicating the role played by the electric dipole LSPs comprising the delocalized LPP mode at $K_{||} = 0$. Interestingly, absorption and LEEG observables each capture the contracted spatial

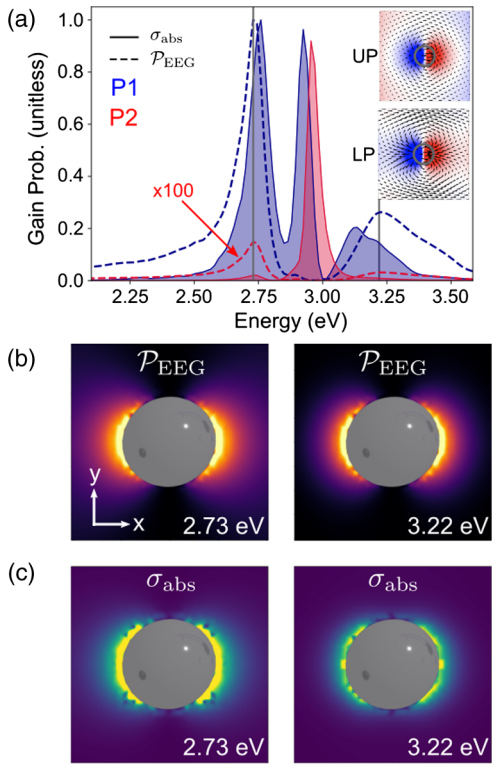

FIG. 4. Spatially and spectrally resolving variations in LPP EPs using LEEG spectroscopy. (a) Normalized relative energy gain and absorption spectra at P1 and P2 from Fig. 3(a) for the array-slab system ($f = 0.0445$, $K_{||} = 0$). Insets show the in-plane electric response field for the combined array-slab system at the UP and LP energies marked by vertical gray lines. The color map corresponds to the out-of-plane component of the response field. (b) $\mathcal{P}_{EEG}$ spectrum images at the UP and LP energies. (c) Point absorption spectrum images at the UP and LP energies.

extent of the UP relative to that of the LP. We attribute this difference to the in-phase (out-of-phase) coupling between the LSP and slab modes at the LP (UP) energy as indicated by the electric field distributions in the insets in Fig. 4(a). By fitting the decay profiles of the normalized absorption and LEEG observables in Figs. 4(b) and 4(c) along the x direction to a monoexponential function (SM), we find that the $1/e$ decay lengths of the LEEG spectrum image UP and LP are 63.19 nm and 70.79 nm—both ∼14% larger than the decay constants of the absorption spectral images. Therefore, despite measuring a scattering response, LEEG measurements are a reliable reporter of the subdiffraction-limited spatial variation of UPs and LPs at the nanometer scale.

STEM EEL spectroscopy has recently emerged as a critical method capable of probing LSP EPs on their natural energy and subdiffraction-limited length scales [34,35]. While this technique has been employed to study EPs based on dispersionless LSPs, here we have shown that it is inadequate for characterizing periodic systems exhibiting strong energy-momentum dispersion. This work establishes weak-field continuous-wave laser-stimulated LEEG spectroscopy as a viable alternative that provides a unique combination of high spatial, spectral, and momentum resolution for characterizing such systems. Although LEEG spectroscopy ultimately measures a scattering response, our numerical calculations indicate LEEG measurements are reliable reporters of subdiffraction-limited spatial variation of LPP EPs features, overestimating extents based on local absorption measurements by ∼14%. We anticipate LEEG measurements will constitute a significant expansion to the existing toolbox used to study EPs in systems with discrete periodicity such as the lattice plasmon systems considered here as well as other structured cavity architectures. Properties such as the spatial-dependence of EP formation, propagation, the role of crystal defects, and EP condensation represent just a few key examples where current understanding will be enhanced and broadened by employing LEEG measurements.

Recently we became aware of a related work [57] that uses photon-induced near-field electron microscopy (PINEM) to probe excitations of periodic photonic crystals in the absence of emitter media.

This research was supported by the National Science Foundation under Grants No. CHE-1954393 and No. QII-TAQS-1936100. The numerical simulations were facilitated through the use of the advanced computational, storage, and networking infrastructure provided by the University of Washington.

*masiello@uw.edu

[1] H. Deng, G. Weihs, C. Santori, J. Bloch, and Y. Yamamoto, Science **298**, 199 (2002).
[2] J. Kasprzak, M. Richard, S. Kundermann, A. Baas, P. Jeambrun, J. M. J. Keeling, F. Marchetti, M. Szymańska, R. André, J. Staehli *et al.*, Nature (London) **443**, 409 (2006).
[3] A. Amo, J. Lefrère, S. Pigeon, C. Adrados, C. Ciuti, I. Carusotto, R. Houdré, E. Giacobino, and A. Bramati, Nat. Phys. **5**, 805 (2009).
[4] A. Amo, T. Liew, C. Adrados, R. Houdré, E. Giacobino, A. Kavokin, and A. Bramati, Nat. Photonics **4**, 361 (2010).
[5] D. Ballarini, M. De Giorgi, E. Cancellieri, R. Houdré, E. Giacobino, R. Cingolani, A. Bramati, G. Gigli, and D. Sanvitto, Nat. Commun. **4**, 1778 (2013).
[6] A. V. Zasedatelev, A. V. Baranikov, D. Urbonas, F. Scafirimuto, U. Scherf, T. Stöferle, R. F. Mahrt, and P. G. Lagoudakis, Nat. Photonics **13**, 378 (2019).
[7] E. Orgiu, J. George, J. Hutchison, E. Devaux, J. Dayen, B. Doudin, F. Stellacci, C. Genet, J. Schachenmayer, C. Genes *et al.*, Nat. Mater. **14**, 1123 (2015).
[8] F. Herrera and F. C. Spano, Phys. Rev. Lett. **116**, 238301 (2016).
[9] R. F. Ribeiro, L. A. Martínez-Martínez, M. Du, J. Campos-Gonzalez-Angulo, and J. Yuen-Zhou, Chem. Sci. **9**, 6325 (2018).

[10] J. Feist, J. Galego, and F. J. Garcia-Vidal, ACS Photonics **5**, 205 (2018).
[11] F. J. Garcia-Vidal, C. Ciuti, and T. W. Ebbesen, Science **373**, eabd0336 (2021).
[12] A. Thomas, L. Lethuillier-Karl, K. Nagarajan, R. M. Vergauwe, J. George, T. Chervy, A. Shalabney, E. Devaux, C. Genet, J. Moran, and T. W. Ebbesen, Science **363**, 615 (2019).
[13] I. Vurgaftman, B. S. Simpkins, A. D. Dunkelberger, and J. C. Owrutsky, J. Phys. Chem. Lett. **11**, 3557 (2020).
[14] M. V. Imperatore, J. B. Asbury, and N. C. Giebink, J. Chem. Phys. **154**, 191103 (2021).
[15] X. Li, A. Mandal, and P. Huo, Nat. Commun. **12**, 1315 (2021).
[16] V. W. Brar, M. C. Sherrott, and D. Jariwala, Chem. Soc. Rev. **47**, 6824 (2018).
[17] D. G. Baranov, M. Wersall, J. Cuadra, T. J. Antosiewicz, and T. Shegai, ACS Photonics **5**, 24 (2018).
[18] R. Chikkaraddy, B. De Nijs, F. Benz, S. J. Barrow, O. A. Scherman, E. Rosta, A. Demetriadou, P. Fox, O. Hess, and J. J. Baumberg, Nature (London) **535**, 127 (2016).
[19] S. Zou, N. Janel, and G. C. Schatz, J. Chem. Phys. **120**, 10871 (2004).
[20] V. G. Kravets, A. V. Kabashin, W. L. Barnes, and A. N. Grigorenko, Chem. Rev. **118**, 5912 (2018).
[21] C. Cherqui, M. R. Bourgeois, D. Wang, and G. C. Schatz, Acc. Chem. Res. **52**, 2548 (2019).
[22] R. Guo, T. K. Hakala, and P. Törmä, Phys. Rev. B **95**, 155423 (2017).
[23] A. Salomon, R. J. Gordon, Y. Prior, T. Seideman, and M. Sukharev, Phys. Rev. Lett. **109**, 073002 (2012).
[24] A. Väkeväinen, R. Moerland, H. Rekola, A.-P. Eskelinen, J.-P. Martikainen, D.-H. Kim, and P. Törmä, Nano Lett. **14**, 1721 (2014).
[25] S. Rodriguez and J. G. Rivas, Opt. Express **21**, 27411 (2013).
[26] S. R. K. Rodriguez, Y. T. Chen, T. P. Steinbusch, M. A. Verschuuren, A. F. Koenderink, and J. G. Rivas, Phys. Rev. B **90**, 235406 (2014).
[27] L. Shi, T. K. Hakala, H. T. Rekola, J.-P. Martikainen, R. J. Moerland, and P. Törmä, Phys. Rev. Lett. **112**, 153002 (2014).
[28] W. Liu, B. Lee, C. H. Naylor, H.-S. Ee, J. Park, A. C. Johnson, and R. Agarwal, Nano Lett. **16**, 1262 (2016).
[29] R. K. Yadav, M. R. Bourgeois, C. Cherqui, X. G. Juarez, W. Wang, T. W. Odom, G. C. Schatz, and J. K. Basu, ACS Nano **14**, 7347 (2020).
[30] H. Lee, I. Kim, C. Park, M. Kang, J. Choi, K.-Y. Jeong, J. Mun, Y. Kim, J. Park, M. B. Raschke *et al.*, Adv. Funct. Mater. **31**, 2102893 (2021).
[31] S. Dai, Z. Fei, Q. Ma, A. Rodin, M. Wagner, A. McLeod, M. Liu, W. Gannett, W. Regan, K. Watanabe *et al.*, Science **343**, 1125 (2014).
[32] M. B. Lundeberg, Y. Gao, R. Asgari, C. Tan, B. Van Duppen, M. Autore, P. Alonso-González, A. Woessner, K. Watanabe, T. Taniguchi *et al.*, Science **357**, 187 (2017).
[33] F. Hu, Y. Luan, M. Scott, J. Yan, D. Mandrus, X. Xu, and Z. Fei, Nat. Photonics **11**, 356 (2017).
[34] A. Konečná, T. Neuman, J. Aizpurua, and R. Hillenbrand, ACS Nano **12**, 4775 (2018).
[35] A. B. Yankovich, B. Munkhbat, D. G. Baranov, J. Cuadra, E. Olsén, H. Lourenço-Martins, L. H. Tizei, M. Kociak, E. Olsson, and T. Shegai, Nano Lett. **19**, 8171 (2019).
[36] P. E. Batson and J. Silcox, Phys. Rev. B **27**, 5224 (1983).
[37] P. Shekhar, M. Malac, V. Gaind, N. Dalili, A. Meldrum, and Z. Jacob, ACS Photonics **4**, 1009 (2017).
[38] F. S. Hage, R. J. Nicholls, J. R. Yates, D. G. McCulloch, T. C. Lovejoy, N. Dellby, O. L. Krivanek, K. Refson, and Q. M. Ramasse, Sci. Adv. **4**, eaar7495 (2018).
[39] J. Hong, R. Senga, T. Pichler, and K. Suenaga, Phys. Rev. Lett. **124**, 087401 (2020).
[40] S. J. Smith and E. Purcell, Phys. Rev. **92**, 1069 (1953).
[41] F. J. García de Abajo, Rev. Mod. Phys. **82**, 209 (2010).
[42] A. Howie, in *Institute of Physics Conference Series* (Adam Hilger, Ltd., Bristol, 1999), Vol. 161, pp. 311–314.
[43] F. J. García de Abajo and M. Kociak, New J. Phys. **10**, 073035 (2008).
[44] A. Asenjo-Garcia and F. J. García de Abajo, New J. Phys. **15**, 103021 (2013).
[45] R. Sapienza, T. Coenen, J. Renger, M. Kuttge, N. F. van Hulst, and A. Polman, Nat. Mater. **11**, 781 (2012).
[46] C. I. Osorio, T. Coenen, B. J. Brenny, A. Polman, and A. F. Koenderink, ACS Photonics **3**, 147 (2016).
[47] S. Peng, N. J. Schilder, X. Ni, J. Van De Groep, M. L. Brongersma, A. Alù, A. B. Khanikaev, H. A. Atwater, and A. Polman, Phys. Rev. Lett. **122**, 117401 (2019).
[48] B. T. Draine and P. J. Flatau, J. Opt. Soc. Am. A **25**, 2693 (2008).
[49] T. J. Antosiewicz, S. P. Apell, and T. Shegai, ACS Photonics **1**, 454 (2014).
[50] S. Prasad and R. J. Glauber, Phys. Rev. A **82**, 063805 (2010).
[51] M. Pelton, S. D. Storm, and H. Leng, Nanoscale **11**, 14540 (2019).
[52] K. D. Heylman, N. Thakkar, E. H. Horak, S. C. Quillin, C. Cherqui, K. A. Knapper, D. J. Masiello, and R. H. Goldsmith, Nat. Photonics **10**, 788 (2016).
[53] N. Thakkar, M. T. Rea, K. C. Smith, K. D. Heylman, S. C. Quillin, K. A. Knapper, E. H. Horak, D. J. Masiello, and R. H. Goldsmith, Nano Lett. **17**, 6927 (2017).
[54] F. Pan, K. C. Smith, H. L. Nguyen, K. A. Knapper, D. J. Masiello, and R. H. Goldsmith, Nano Lett. **20**, 50 (2019).
[55] K. C. Smith, A. Olafsson, X. Hu, S. C. Quillin, J. C. Idrobo, R. Collette, P. D. Rack, J. P. Camden, and D. J. Masiello, Phys. Rev. Lett. **123**, 177401 (2019).
[56] See Supplemental Material at http://link.aps.org/supplemental/10.1103/PhysRevLett.128.197401 for information on mathematical derivations and companion numerical simulations describing: (1) optical 1D array excitation, (2) STEM electron energy loss—1D arrays, (3) electron energy gain probability —1D arrays, (4) evaluation of 1D lattice sum tensor elements, (5) numerical evaluation of the electron energy gain probability, (6) empty-lattice dispersion relation in dispersive background media, (7) normalization procedure for spatial maps in Fig. 4, and (8) profiles of the upper and lower exciton-polariton electric fields within the excitonic medium.
[57] K. Wang, R. Dahan, M. Shentcis, Y. Kauffmann, A. B. Hayun, O. Reinhardt, S. Tsesses, and I. Kaminer, Nature (London) **552**, 50 (2020).